Molecular identification of HSPA8 as an accessory protein of a hyperpolarization-activated chloride channel from rat pulmonary vein cardiomyocytes

Received for publication, January 5, 2019, and in revised form, August 28, 2019 Published, Papers in Press, September 10, 2019, DOI 10.1074/jbc.RA119.007416

Yosuke Okamoto[‡], **Yoshinobu Nagasawa**[§], **Yutaro Obara**[¶], **Kuniaki Ishii**[¶], **Daichi Takagi**[‡], **and Kyoichi Ono**[‡1]

From the [‡]*Department of Cell Physiology, Akita Graduate School of Medicine, 1-1-1 Hondo, Akita 010-8543, Japan, the* [§]*Department of Pharmacology and Therapeutics, Faculty of Pharmaceutical Sciences, Toho University, Chiba 274-8510, Japan, and the* [¶]*Department of Pharmacology, Yamagata University Faculty of Medicine, 2-2-2 Iida-nishi, Yamagata 990-9585, Japan*

Edited by Mike Shipston

Pulmonary veins (PVs) are the major origin of atrial fibrillation. Recently, we recorded hyperpolarization-activated Cl^- current ($I_{Cl,h}$) in rat PV cardiomyocytes. Unlike the well-known chloride channel protein 2 (CLCN2) current, the activation curve of $I_{Cl,h}$ was hyperpolarized as the Cl^- ion concentration ($[Cl^-]_i$) increased. This current could account for spontaneous activity in PV cardiomyocytes linked to atrial fibrillation. In this study, we aimed to identify the channel underlying $I_{Cl,h}$. Using RT-PCR amplification specific for *Clcn2* or its homologs, a chloride channel was cloned from rat PV and detected in rat PV cardiomyocytes using immunocytochemistry. The gene sequence and electrophysiological functions of the protein were identical to those previously reported for *Clcn2*, with protein activity observed as a hyperpolarization-activated current by the patch-clamp method. However, the $[Cl^-]_i$ dependence of activation was entirely different from the observed $I_{Cl,h}$ of PV cardiomyocytes; the activation curve of the *Clcn2*-transfected cells shifted toward positive potential with increased $[Cl^-]_i$, whereas the $I_{Cl,h}$ of PV and left ventricular cardiomyocytes showed a leftward shift. Therefore, we used MS to explore the possibility of additional proteins interacting with CLCN2 and identified an individual 71-kDa protein, HSPA8, that was strongly expressed in rat PV cardiomyocytes. With co-expression of HSPA8 in HEK293 and PC12 cells, the CLCN2 current showed voltage-dependent activation and shifted to negative potential with increasing $[Cl^-]_i$. Molecular docking simulations further support an interaction between CLCN2 and HSPA8. These findings suggest that CLCN2 in rat heart contains HSPA8 as a unique accessory protein.

Ectopic excitability originating in pulmonary veins (PVs)[2] causes symptomatic atrial fibrillation (AF) (1, 2). A number of researchers have recorded spontaneous excitability in isolated PV tissues. Several potential causes of spontaneous activity have been reported in these cases, including independent pacemaking activity in muscular tunics of guinea pig PVs (3), α- and β-adrenergic stimulation by noradrenaline (3–5), Ca^{2+} overload in intracellular storage sites induced by digitalis (6), and intracellular Ca^{2+} leakage (7). The progression of atrial fibrosis is also considered to be an essential factor in structural remodeling in AF (8–12). Genome-wide analysis indicated that chromosomal loci associated with Ca^{2+}-activated K^+ channels and hyperpolarization-activated cation channels are linked to AF (13). Furthermore, transient receptor potential channel 3 protein expressed in atrial fibroblasts is also involved in structural remodeling of the atria (14). In addition, we previously identified a hyperpolarization-activated Cl^- current ($I_{Cl,h}$) that appears to be involved in the ectopic automaticity of rat PV cardiomyocytes (15).

Several types of Cl^- channels, including the cAMP-activated cystic fibrosis transmembrane conductance regulator (CFTR) (16), the Ca^{2+}-activated Cl^- channel (17), and the hyperpolarization-activated chloride channel protein 2 (CLCN2) channel (18), have been identified in mammalian cardiomyocytes. CLCN2 is activated by both hyperpolarization and hypoosmotic stress. Interestingly, Duan *et al.* (19) detected a minor splice variant of CLCN2 that is unique to the rat heart. However, like the full-length protein, this variant was activated by both hyperpolarization and hypoosmolality. In contrast, $I_{Cl,h}$ was accepted as a novel type of hyperpolarization-activated Cl^- current, because its response to intracellular Cl^- and extracellular osmolarity differed from those of CLCN2 (15).

In this study, we attempted to identify the Cl^- channel responsible for $I_{Cl,h}$ using a molecular cloning and proteomic analysis-based approach. Our results revealed that a member of the heat-shock protein (HSP) 70 superfamily, HSPA8, acts as an auxiliary protein of the CLCN2 Cl^- channel. Thus, we propose that CLCN2, in association with HSPA8, is a leading candidate for the molecular architecture underlying $I_{Cl,h}$.

This work was supported by JSPS KAKENHI (Grant-in-Aid for Research Activity Start-up Grant Number JP15H06006 to Y. Okamoto, and Grant-in-Aid for Young Scientists (B) Grant Number JP17H15554 to Y. Okamoto) by a grant-in-aid from the Nishinomiya Basic Research Foundation of Japan (to Y. Okamoto), and by collaboration with Ono Pharmaceutical Cooperation, Ltd. (Japan). The authors declare that they have no conflicts of interest with the contents of this article.

This article contains Figs. S1–S4.

[1] To whom correspondence should be addressed. Tel.: 81-18-884-6070; Fax: 81-18-836-2604; E-mail: onok@med.akita-u.ac.jp.

[2] The abbreviations used are: PV, pulmonary vein; AF, atrial fibrillation; CFTR, cystic fibrosis transmembrane conductance regulator; LV, left ventricle; ANOVA, analysis of variance; RyR, ryanodine; HRP, horseradish peroxidase; GAPDH, glyceraldehyde-3-phosphate dehydrogenase.

Table 1
List of cloning primers
The top pair of primers was used in the cloning of full-length rat *Clcn2*. The lower pair was used in the subcloning of rat *Hspa8*. The restriction enzyme cutting sites are indicated in lowercase characters.

Primer name	Sequences (5′–3′)
Full_rClcn2_F	5′-ACAaagcttAGAAGCAAGAGGAGGCAAGAGG-3′
Full_rClcn2_R	5′-ACACAgaattcCTTCTGGTCACTGCTGGCTTGC-3′
EcoRI–Hspa8–forward	5′-AAgaattcTCTGTGTGGTCTCGTCATCAGC-3′
XbaI–Hspa8–reverse	5′-AAtctagaGGGTCCCTGTGGAACAATGC-3′

Results

Functional cloning of full-length Clcn2 from rat PV cardiomyocytes

To identify a Cl^- channel that could be attributed to the previously reported $I_{Cl,\,h}$ in rat PV cardiomyocytes (15), we attempted to isolate cDNA corresponding to the Cl^- channel by RT-PCR. Total RNA extracted from rat PV cardiomyocytes was reverse-transcribed and amplified using a set of specific primers (Full_rClcn2_F/Full_rClcn2_R, Table 1). Based on the hypothesis that the Cl^- channel-encoding gene of interest should be homologous to *Clcn2*, the primers were designed to span the region encompassing the start and end codons of *Clcn2* (*i.e.* the complete coding sequence). As shown in Fig. 1*A*, the reverse transcript from the small intestine indicated that the intrinsic full-length *Clcn2* gene was 2811 bp in length. Transcripts from PV cardiomyocytes were apparently identical in size to this *Clcn2* sequence. Gel bands corresponding to the *Clcn2* cDNA amplicons transcribed from PVs were digested, purified, and inserted into the pcDNA3.1 expression vector using appropriate restriction enzymes. Sanger sequencing confirmed that the inserted cDNA sequences were identical to the published *Clcn2* sequence (Fig. S1). The smaller transcripts below the *Clcn2* bands (Fig. 1*A*) are products of nonspecific amplification.

The electrophysiological properties of the cloned *Clcn2* gene were analyzed in HEK293 cells using the patch-clamp method. Without CLCN2 transfection, time-dependent current was negligible (Fig. S2*A*). To evaluate the effects of different Cl^- ion concentrations ($[Cl^-]_i$) on the voltage-gating, steady-state activation under various $[Cl^-]_i$ values (40, 100, or 150 mM) was analyzed by measuring the amplitude of the tail current at 40 mV. The relationship between the test potentials and the relative amplitude of the tail current was fitted with the Boltzmann equation and plotted (Fig. 1*C*). As $[Cl^-]_i$ increased, the steady-state activation curves shifted toward positive potential and maintained similar slopes. The $V_{1/2}$ and the slope factors were -72.3 ± 6.6 and -29.6 ± 3.3 mV, respectively, at a $[Cl^-]_i$ of 40 mM ($n = 5$), -58.3 ± 15.4 and -30.6 ± 9.5 mV, respectively, at a $[Cl^-]_i$ of 100 mM ($n = 7$), and -52.1 ± 10.4 and -28.3 ± 7.2 mV, respectively, at a $[Cl^-]_i$ of 150 mM ($n = 7$) (Fig. 1, *D* and *E*). There was a statistically significant difference in $V_{1/2}$ (Kruskal-Wallis test, $p = 0.0025$) but no difference in slope factors. These results are consistent with previous reports (20). The time course of activation is summarized in Fig. 1*F* with fast and slow time constants (τ_{fast} and τ_{slow}). In some cases, the time constants had to be interfered with by the apparent inactivation, most likely as a result of Cl^- depletion.

Cell localization of CLCN2 in rat PV and LV cardiomyocytes

CLCN2 is reported to be expressed in the rat left ventricle (LV) (21). We confirmed the cellular localization of CLCN2 in LV and PV cardiomyocytes using immunocytochemistry. Fig. 2 shows representative confocal images of cardiomyocytes isolated from these tissues and labeled with a set of CLCN2 (*green*) and Na-K pump (*red*), or RyR (*green*) and CLCN2 (*red*) antibodies. Immunostaining of the Na-K pump indicates a plasma membrane pattern, whereas RyR represents a typical cell structure of cardiomyocyte. Overlay image of CLCN2 with Na/K pump reveals that the Cl^- channel expresses the cell surface in addition to intracellular spaces. CLCN2 is also expressed in the periphery of LV myocyte.

Hyperpolarization-activated Cl^- current in rat LV cardiomyocytes

Next, we examined whether the Cl^- current in LV myocytes also exhibited $I_{Cl,\,h}$-like properties. The effects of different $[Cl^-]_i$ (40, 100, or 150 mM; $n = 8$, 7, and 6 for each, respectively) on voltage-gating were evaluated using the patch-clamp method. As $[Cl^-]_i$ increased, the steady-state activation curves shifted toward negative potential with more gradual slopes. The $V_{1/2}$ and the slope factors were -75.0 ± 7.4 and -15.7 ± 5.5 mV, respectively, at a $[Cl^-]_i$ of 40 mM and -89.4 ± 10.2 and -22.2 ± 5.5 mV, respectively, at a $[Cl^-]_i$ of 100 mM and -104.3 ± 10.8 and -26.2 ± 7.1 mV, respectively, and at a $[Cl^-]_i$ of 150 mM (Fig. 3, *B–D*). The values of both $V_{1/2}$ and slope factor were decreased as $[Cl^-]_i$ increased. The time course of activation at -120 mV was analyzed by fitting the data to a first-order biexponential function. Both τ_{slow} and τ_{fast} were plotted (Fig. 3*E*). τ_{slow} values were 1346.6 ± 1150.0, 915.4 ± 869.5, and 636.5 ± 489.8 ms of $[Cl^-]_i$ and 40, 100, and 150 mM, respectively (Fig. 3*E*, *open circles*). The τ_{fast} values were 114.9 ± 35.9, 55.7 ± 20.3, and 55.8 ± 10.9 ms at $[Cl^-]_i$ and 40, 100, and 150 mM, respectively (Fig. 3*E*, *filled circles*), and significantly decreased by increasing $[Cl^-]_i$ ($p = 0.004$).

Molecular identification of HSPA8 as an accessory protein of CLCN2

The electrophysiological function of endogenous CLCN2 in rat LV and PV cardiomyocytes was observed as $I_{Cl,\,h}$. The observed $[Cl^-]_i$-dependent gating of $I_{Cl,\,h}$ was largely different from the properties of the well-known CLCN2 current (ClC-2). When *Clcn2* is introduced alone in HEK293 cells, the steady-state activation curve of ClC-2 shifts toward positive potential with increasing $[Cl^-]_i$ (20, 22). We hypothesized that CLCN2 is regulated by an unidentified molecule, which would modulate the $[Cl^-]_i$ dependence of the channel. We therefore explored CLCN2-binding proteins by immunoprecipitation. Solubilized membrane proteins from rat PV and LV cardiomyocytes were precipitated with an anti-CLCN2 antibody and separated by electrophoresis. Precipitants were detected at ~90, ~70, ~50, and ~25 kDa on Coomassie-stained gels (Fig. 4*A*). CLCN2 was identified as the band running at ~90 kDa. A band of weak intensity at ~180 kDa was presumed to be residual CLCN2 dimer. Bands at ~50 and ~25 kDa are consistent with the heavy and light chains of immunoglobulin used in the immunoprecipitation.

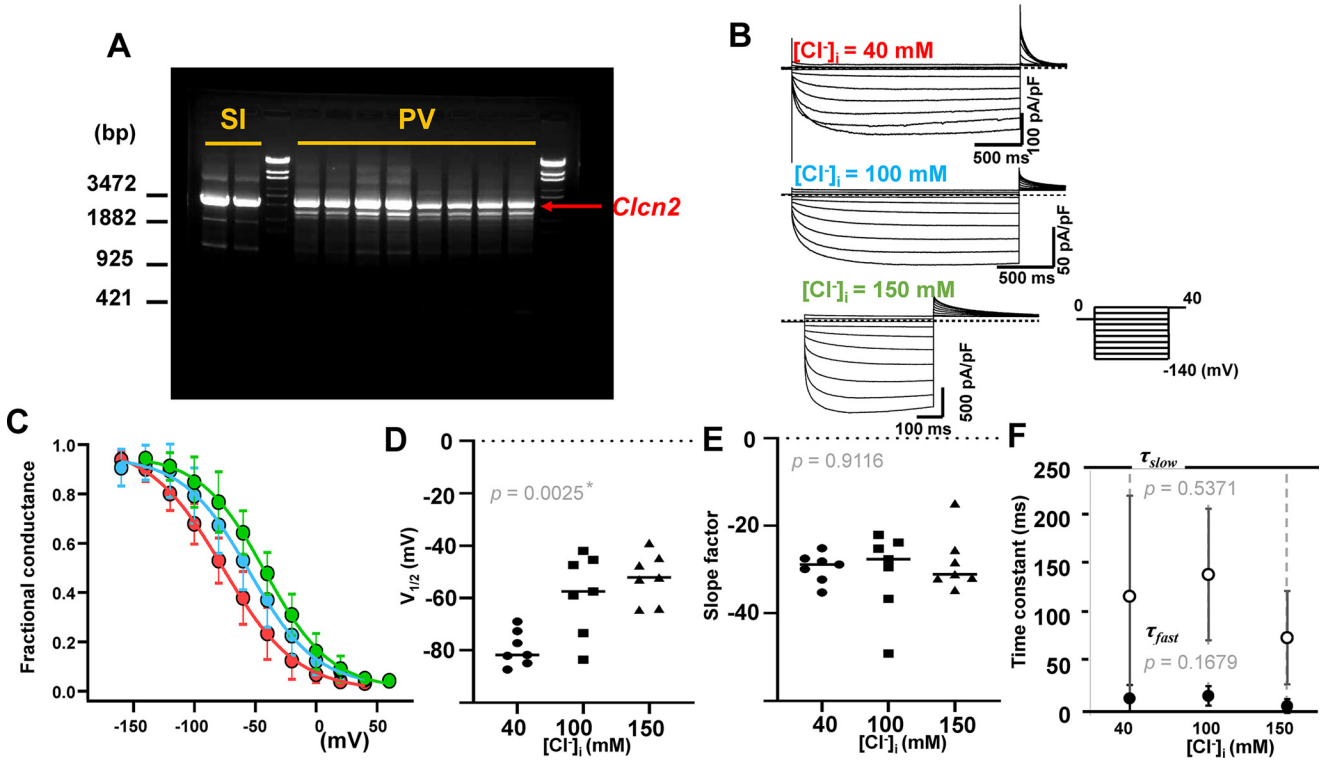

Figure 1. Functional cloning of *Clcn2* from rat PV. *A,* detection of full-length 2811-bp rat *Clcn2* in the small intestine (*SI*), used as a positive control, and in PV. The DNA sizes are indicated on the *left*. The *red arrow* indicates the exact size of CLCN2. Each pair of adjacent lanes is derived from the same rat (*i.e.* the PV of four individual rats is shown on the gel). The two most intense bands in the *middle* of the gel were extracted for gene cloning. *B,* hyperpolarization-activated Cl^- currents of cloned *Clcn2* were recorded under chloride ion concentrations ($[Cl^-]_i$) of 40, 100, and 150 mM, with $[Cl^-]_o$ = 148.9 mM. The pulse protocol is indicated at the *bottom* of the figure. *Dashed lines* indicate current levels of 0. *C,* steady-state activation curves under different $[Cl^-]_i$ evaluated by current amplitudes of tail currents at 40 mV. *Magenta, marine blue,* and *green* indicate data obtained under $[Cl^-]_i$ of 40, 100, and 150 mM, respectively. $n = 7$ for each $[Cl^-]_i$. $V_{1/2}$ and *S* values determined by Boltzmann fitting are plotted against $[Cl^-]_i$ in *D* and *E*, respectively. Statistically significant difference was calculated from Kruskal-Wallis test. *F,* slow (τ_{slow}) and fast (τ_{fast}) time constants at −120 mV obtained by fitting the raw data with a biexponential function are plotted against $[Cl^-]_i$.

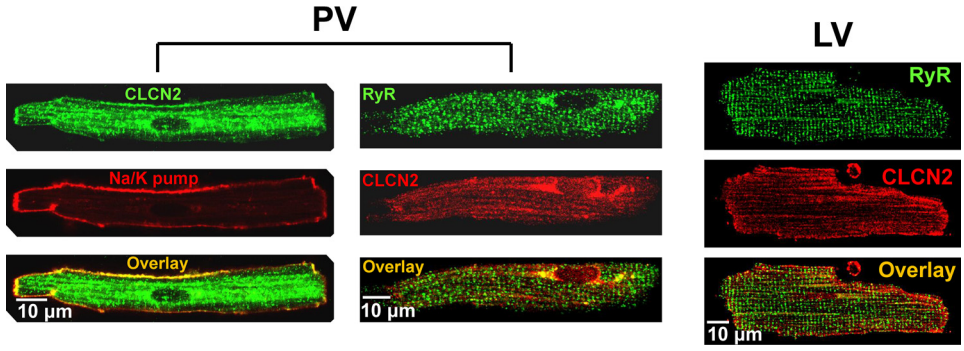

Figure 2. Immunocytochemical analysis of cardiomyocytes isolated from PV (*left, middle*) and LV (*right*). PV myocyte is labeled with a pair of CLCN2 (*green*) and Na/K pump (*red*) and a pair of RyRs (*green*) and CLCN2s (*red*). Immunostaining of Na/K pump performed as a plasma membrane marker, and co-localization between CLCN2 and Na/K pump is indicated by *yellow color* in the overlay image. RyR indicates striated myocardial pattern. LV myocytes are stained with antibodies against RyR and CLCN2.

However, the residual ~70-kDa bands (marked with *arrows* in Fig. 4*A*) are unknown proteins, indicating an accessory protein of CLCN2. These bands were excised, digested with trypsin, and eluted with 0.5% TFA. The eluted peptides were then analyzed using MS. Of the eluted peptides, 62 were identified as being of rat origin (Fig. S3). Only eight of the peptides had been recognized as a part of functional protein, and all corresponded to constitutive heat-shock protein HSPA8 (71 kDa) of rats (Fig. 4*B* and Fig. S3). Immunoblotting of the precipitate indicated that HSPA8 corresponded to the CLCN2-interacting protein (Fig. 4*C*, *left*), and the interaction between HSPA8 and CLCN2 was confirmed by reverse co-immunoprecipitation using an anti-HSPA8 antibody (Fig. 4*C*, *right*). The molecular interaction was confirmed by immunoblotting more than three times in both PV and LV samples. Fig. 4*C* is the representative example. *Hspa8* was abundantly expressed in rat PV cardiomyocytes (Fig. 5*A*) and was successfully subcloned from rat PV cardiomyocytes (Fig. S3) using specific primers (Table 1). Immunocytochemistry discovered that HSPA8 was present on the cell surface of PV and LV cardiomyocytes (Fig. 5, *B* and *C*), implying co-localization with CLCN2.

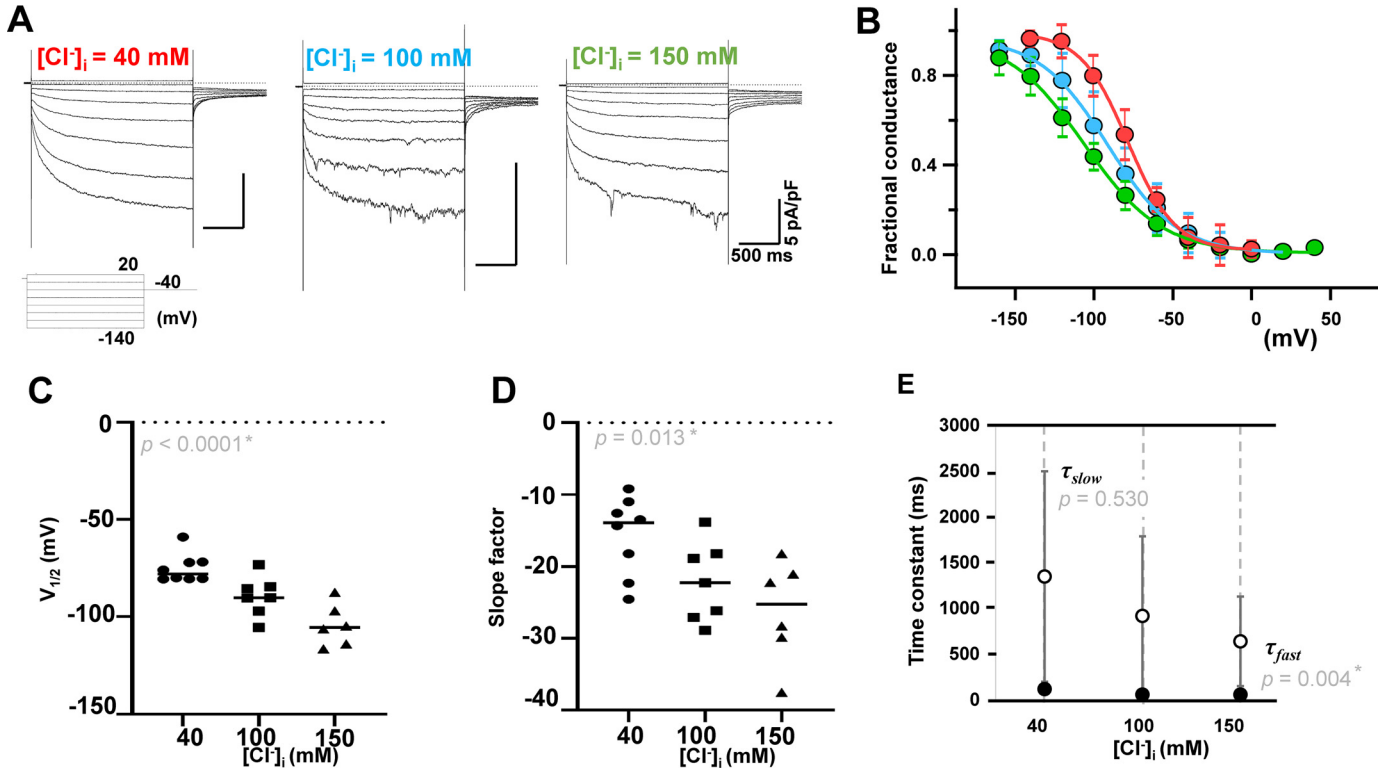

Figure 3. Effect of the chloride ion concentration ($[Cl^-]_i$) on the voltage dependence of the hyperpolarization-activated Cl^- current ($I_{Cl,h}$) in left ventricle cardiomyocytes. *A,* raw traces recorded at $[Cl^-]_i$ of 40, 100, and 150 mM $[Cl^-]_i$, with $[Cl^-]_o$ = 148.9 mM. *Horizontal bars* (500 ms) and *vertical bars* (5 pA/picofarad) are shown for all traces. The pulse protocol is shown. *B,* steady-state activation curves evaluated by tail currents under different $[Cl^-]_i$ at 40 mV. The color-coding is the same as in Fig. 1. $V_{1/2}$ and *S* values are plotted against $[Cl^-]_i$ in *C* and *D*, respectively. *E,* slow (τ_{slow}, *open circles*) and fast (τ_{fast}, *closed circles*) time constants at −120 mV obtained by fitting the raw data with a biexponential function are plotted against $[Cl^-]_i$.

Functional characterization of HSPA8 by patch-clamping in HEK293 and PC12 cells

Cloned *Hspa8* was co-transfected into HEK293 cells with *Clcn2,* and the ClC-2 current was recorded using the conventional whole-cell patch-clamp method (Fig. 6). At a $[Cl^-]_i$ of 40 mM, the $V_{1/2}$ was −71 ± 20.0 mV, and the slope factor was −23.9 ± 3.1 (n = 5). The $V_{1/2}$ was not statistically changed (p = 0.38), while the slope factor was affected by transfection of cloned *Hspa8* (p = 0.03). However, with a $[Cl^-]_i$ of 150 mM, the voltage dependence of the ClC-2 current produced by co-transfected *Hspa8* and *Clcn2* appeared not to fit a single Boltzmann function, but it was satisfactorily approximated by the sum of the two components. The $V_{1/2}$ and slope factor values for one component were −120.4 ± 12.3 and −12.9 ± 6.2 mV, respectively. They were significantly affected by co-transfection of HSPA8 (p = 0.004 for $V_{1/2}$ and p = 0.009 for slope factor with Mann-Whitney test).The $V_{1/2}$ and slope factor values for the other component were −25.1 ± 25.4 and 21.2 ± 8.6 mV, respectively, without a statistically significant difference from those values in the absence of *Hspa8* (p = 0.126 and 0.247 for $V_{1/2}$ and slope factor). The relative magnitudes of the two components are 0.38 ± 0.14 for the former (low voltage) and 0.62 ± 0.14 for the latter (high voltage) components, respectively (n = 5, Fig. 6, *A–C*). Reportedly, rat CLCN2 binds to another heat-shock protein, human HSP90, in HEK293 cells (24). To diminish the effect of human HSP90 on voltage-dependent gating, we carried out an identical patch-clamp protocol using the rat-derived cell line PC12. The cells are known to possesses voltage-gated K^+ currents (25), while the Cl^- current was undetectable as indicated in Fig. S2*B*. When *Clcn2* was transfected alone into PC12 cells, the $V_{1/2}$ and slope factor values of the ClC-2 current were −55. 1 ± 9.4 and −19.5 ± 1.8 mV, respectively, at a $[Cl^-]_i$ of 40 mM, and −56.3 ± 24.7 and −22.7 ± 5.9 mV, respectively, at a $[Cl^-]_i$ of 150 mM (n = 4 for each, Fig. 7, *A–C*). Statistically significant differences between $[Cl^-]_i$ of 40 and 150 mM in both $V_{1/2}$ and slope factor were unobserved. By contrast, when *Hspa8* was overexpressed with *Clcn2* in PC12 cells, the activation curves deviated from a single Boltzmann function and were fitted to the sum of two Boltzmann components, *i.e.* low and high voltage–activated components (Fig. 7, *D–F*). At a $[Cl^-]_i$ of 40 mM (n = 6), the $V_{1/2}$ and slope factor values of the low voltage–activated component were −110.9 ± 12.7 and −14.9 ± 7.9 mV, respectively. The values for the high voltage–activated component were −40.3 ± 23.5 and −14.8 ± 3.0 mV, respectively. When $[Cl^-]_i$ was increased to 150 mM (n = 5), the activation of the low voltage–activated component shifted toward negative potential (p = 0.002). The $V_{1/2}$ and slope factor values of the low voltage–activated component at a $[Cl^-]_i$ of 150 mM were −182.0 ± 13.6 and −22.9 ± 6.1 mV, respectively, whereas those of the high voltage–activated component were −17.1 ± 10.2 and −12.5 ± 4.5 mV, respectively. Statistical analysis revealed that the $V_{1/2}$ of low-voltage component after the co-transfection was substantially shifted toward negative potential by increasing $[Cl^-]_i$ (p = 0.002), while the other component was unaffected (p = 0.09). The relative magnitudes of the low voltage–activated component are overviewed in

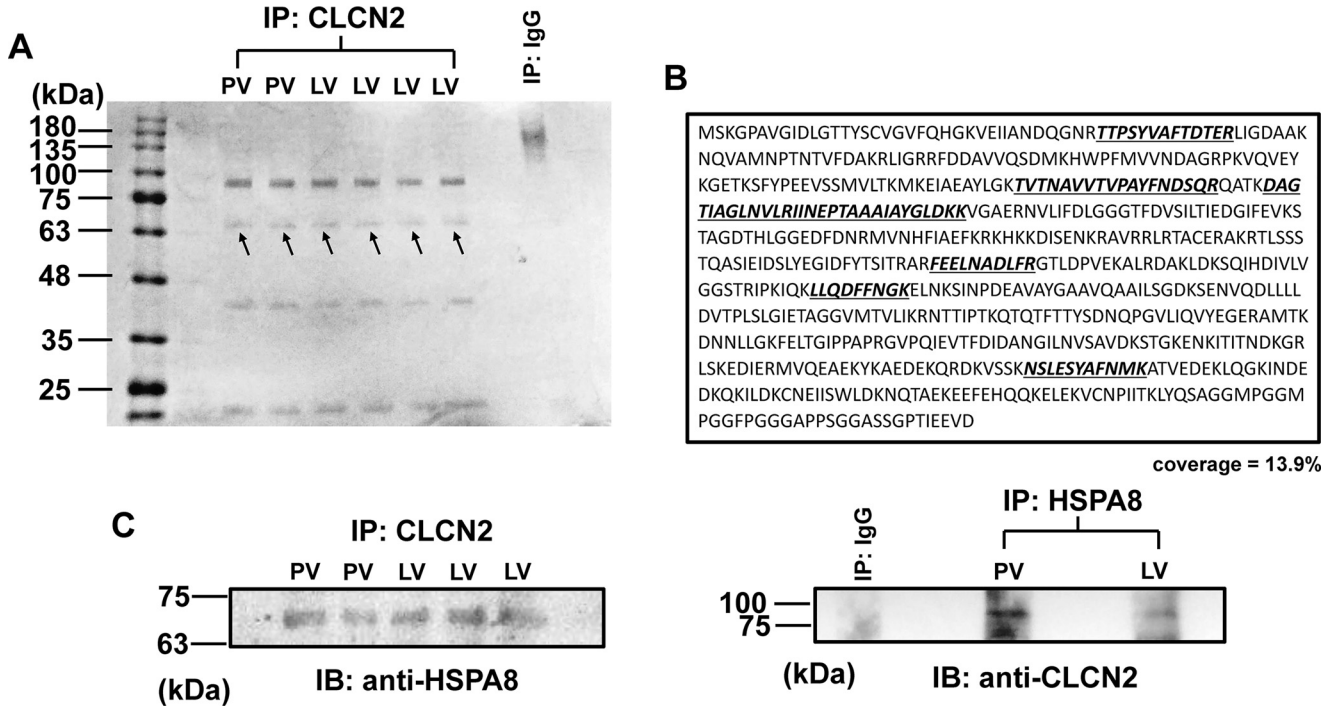

Figure 4. Identification of HSPA8 as a CLCN2-interacting protein. *A,* detection of CLCN2-interacting proteins in the membrane fraction by Coomassie Brilliant Blue staining. The membrane protein fractions from lysed PV and LV cardiomyocytes were immunologically purified by co-immunoprecipitation (*IP*) using an anti-CLCN2 antibody and separated by SDS-PAGE. Protein size is indicated on the *left*. CLCN2 and immunoglobulin heavy and light chain proteins were detected at ~90, 50, and 25 kDa, respectively. The protein at ~70 kDa (indicated with *arrows*) is an unidentified molecule. Precipitant with 10 μg of mouse IgG was loaded in as a negative control. *B,* determination of the amino acid sequence of the unknown molecule by LC-tandem MS analysis. Mass spectrometry analysis identified eight peptides of rat origin, all of which corresponded to a single protein, HSPA8. The complete 646-amino acid sequence of HSPA8 is displayed. The 90 amino acids used in the identification of the eight peptides are indicated in *bold, underlined, italic characters*. Coverage was calculated as the ratio of the identified 90 amino acids to the 646 total amino acids. *C,* confirmation of the protein–protein interaction. Precipitants obtained from the crude membrane fractions of PV or LV using either CLCN2 (*left panel*) or HSPA8 (*right panel*) antibody are blotted with the other antibody. Origins of loaded proteins (*i.e.* PV or LV) are indicated *above* the corresponding gel lanes. Precipitant with 10 μg of rabbit IgG was also loaded as a negative control on the *right panel*. *IB*, immunoblot.

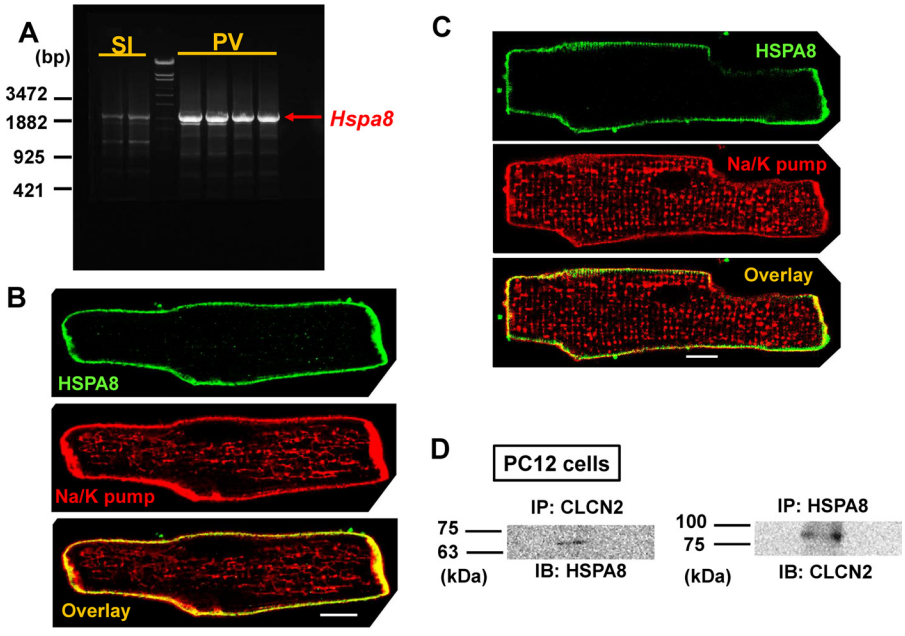

Figure 5. Expression and localization of *Hspa8* in cardiomyocytes. *A,* RT-PCR detects full-length 2027-bp *Hspa8* (*SI*; small intestine). The cDNA is subcloned. *B,* immunocytochemistry of PV cardiomyocytes against HSPA8 (*green*) and Na/K pump (*red*). Immunostaining of Na/K pump indicates the location of the cell surface. The overlay image (*bottom*) emphasizes co-localization of HSPA8 with the plasma membrane marker. *Scale bar* is 10 μm. *C,* immunocytochemistry of LV cardiomyocytes against HSPA8 (*green*) and Na/K pump (*red*). HSPA8 is located on the cell surfaces. Of note, immunostaining of Na/K pump detects enriched transverse tubule. *Scale bar* is 10 μm. *D,* immunoprecipitants in PC12 cells reconfirm the interaction between cloned CLCN2 and HSPA8 again. *IP*, immunoprecipitation; *IB*, immunoblot.

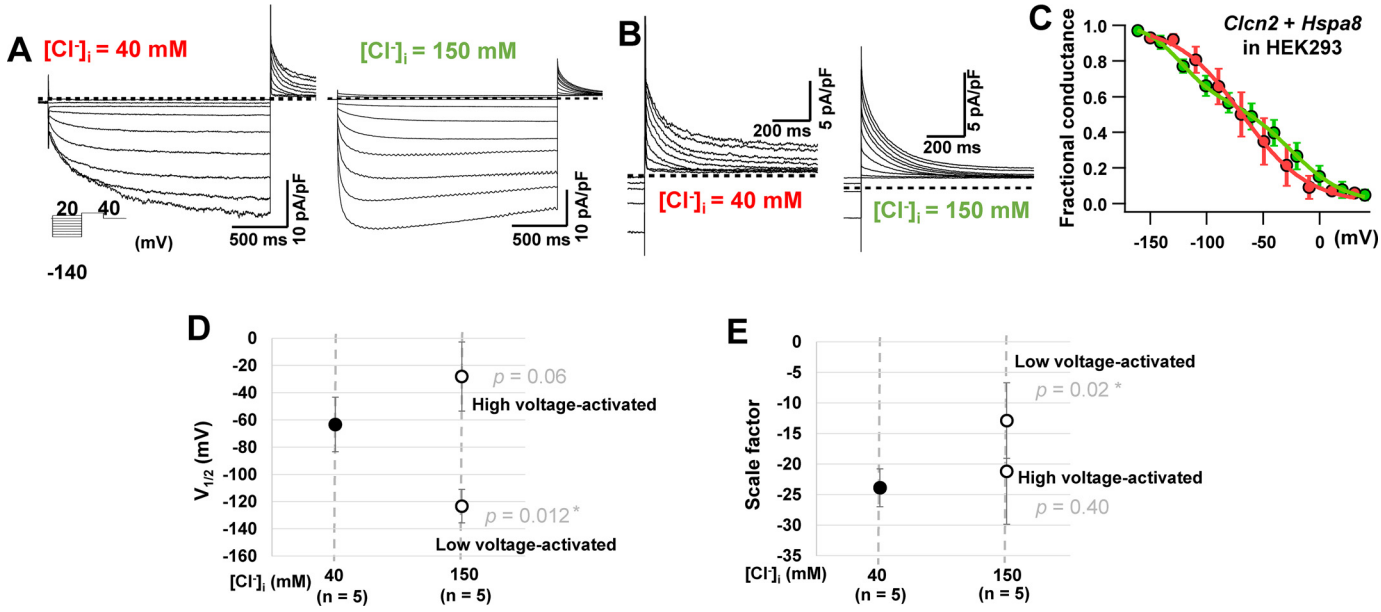

Figure 6. Effect of *Hspa8* expression on the chloride ion concentration ($[Cl^-]_i$)-dependent voltage-gating in HEK293 cells. *Hspa8* was co-transfected with *Clcn2*. *A*, $[Cl^-]_i$ was 40 mM (*left*) and 150 mM (*right*). The pulse protocol is shown in the *inset*. Activation curves were evaluated based on the amplitude of tail currents at 40 mV. The initial portion of the tail current is shown in expanded scale in *B*. Experimental results are summarized by Boltzmann fitting in *C*. $V_{1/2}$ and *S* values are plotted against $[Cl^-]_i$ in *D* and *E*, respectively. Of note, the activation curve at $[Cl^-]_i$ is divided into two components, and the low voltage–activated component is statistically significantly different from the activation curve at 40 mM $[Cl^-]_i$.

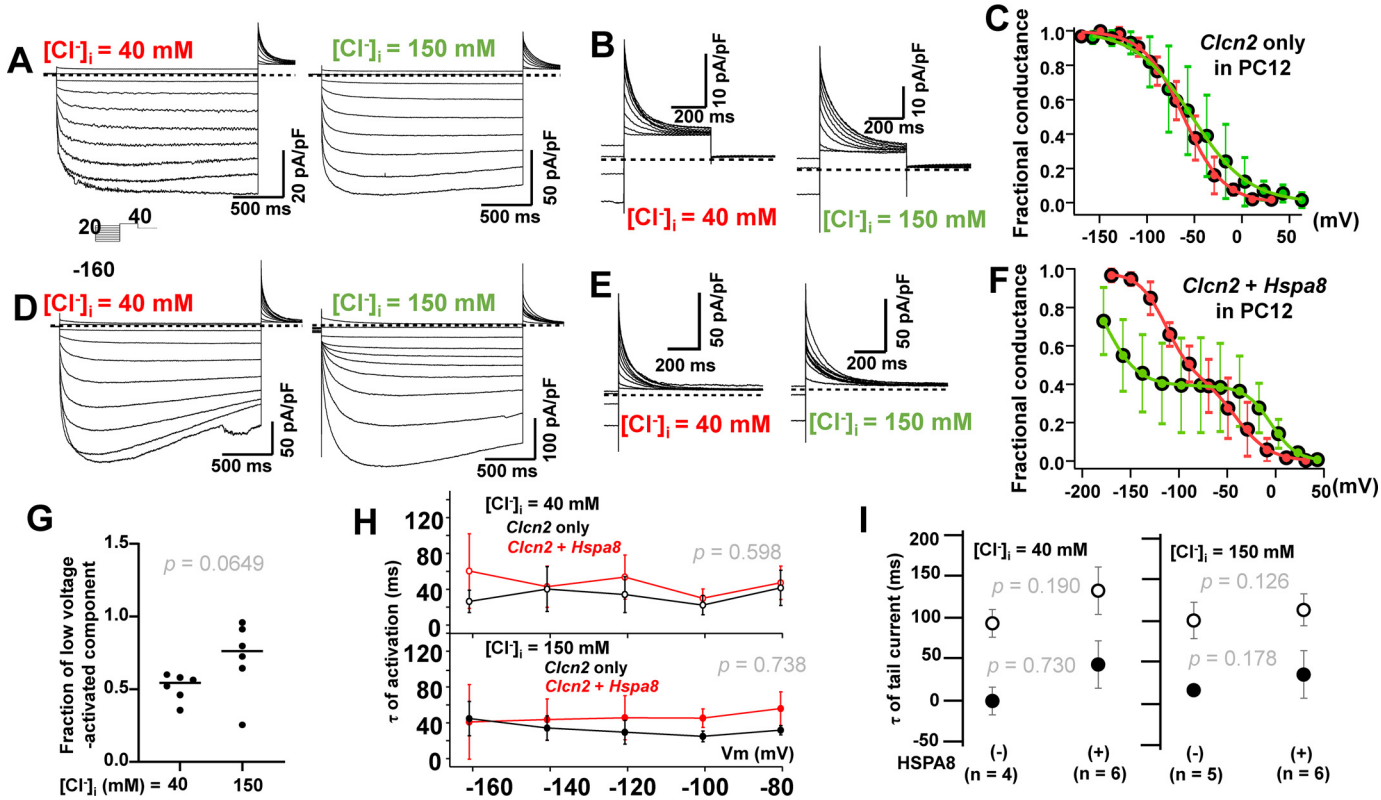

Figure 7. Effect of *Hspa8* overexpression on the $[Cl^-]_i$-dependent voltage-gating in PC12 cells. *A*, chloride ion concentration ($[Cl^-]_i$)-dependent voltage-gating CLCN2 current in PC12 cells without co-transfection of *Hspa8*. Current traces were obtained using the pulse protocol shown in the *inset*. The $[Cl^-]_i$ was 40 mM (*left*) and 150 mM (*right*). Activation curves were evaluated based on the amplitude of tail currents at 40 mV. The tail current is shown in expanded scale in *B*. The color-coding of the results is the same as in Fig. 1. *C*, activation curves are gained by Boltzmann fittings. *D*, CLCN2 current in PC12 cells with co-transfection of *Hspa8*. The pulse protocol is same as *A*. The tail current and activation curve are shown in *E*. The activation curves are fitted with a double-Boltzmann function in *F*, and contributions of the low voltage–activated component are overviewed in *G*. *H*, time constants of the Cl^- currents activated −160 to −80 mV. The currents were evoked in PC12 cells with or without overexpression of *Hspa8* in both conditions of $[Cl^-]_i$ = 40 and 150 mM. The two-way ANOVA undetected impact of *Hspa8* on the value is shown. *I*, τ_{fast} (*closed circles*) and τ_{slow} (*open circles*) of tail currents at 40 mV following activation by hyperpolarization of −160 mV are measured in PC12 cells with or without overexpression of *Hspa8* in both conditions of $[Cl^-]_i$ = 40 and 150 mM.

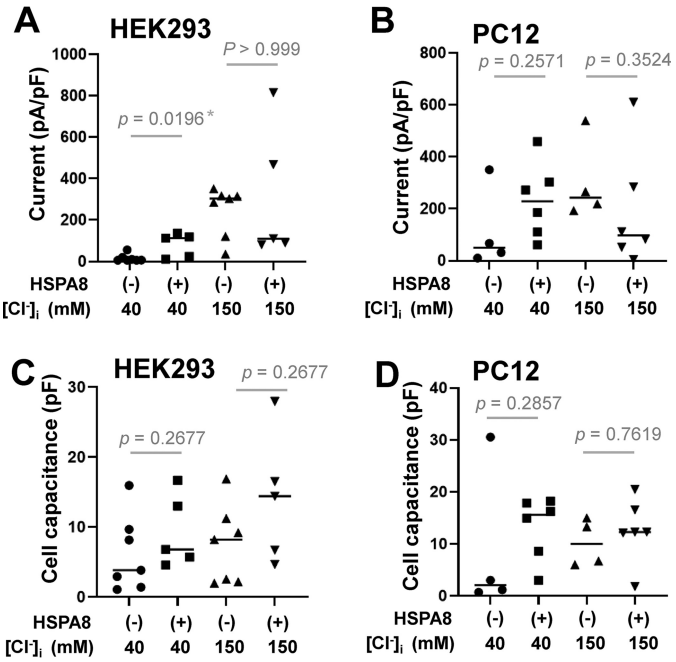

Figure 8. Other electrophysiological parameters for HEK293 and PC12 cells. The amplitudes of the CLCN2 currents were evaluated by tail currents at 40 mV following the hyperpolarization to −120 mV. The data obtained using HEK293 cells are summarized in *A*, and PC12 data are summarized in *B*. The data are classified by experimental conditions, *i.e.* $[Cl^-]_i$, cell type, and co-expression of *Hspa8*, as indicated. *C* and *D* summarize cell capacitance (C_m) of cells. According to the Mann-Whitney test for each experimental condition (cell type and $[Cl^-]_i$), *Hspa8* expression affects current amplitude at 40 mM $[Cl^-]_i$ in HEK293 cells; otherwise, no statistical significance was detected.

Fig. 7*G*. To evaluate the effect of HSPA8 on time-dependent kinetics, we measured the time constant of the activated currents and tail currents subsequent to the activation by hyperpolarization to −160 mV. The influence of the presence or absence of HSPA8 was compared in the both condition of $[Cl^-]_i = 40$ and 150 mM. As a result, there are no significant impact of HSPA8 on the time constants (Fig. 7, *H* and *I*). Electrophysiological properties other than the voltage dependences and time constants were also evaluated (Fig. 8). Consistent effects of *Hspa8* expression were not uncovered in those parameters.

Homology modeling of protein structures and protein–protein docking simulations

To compare the protein–protein docking simulation between CLCN2 and either HSP90 or HSPA8, protein structures of rat CLCN2, rat HSPA8, and human HSP90 were homologically simulated using the homology-modeling server SWISS-MODEL. The Cl^- channel structure from human CLC-1 (26) was used as a template for the model of rat CLCN2. The QMEAN score and sequence identity of the model were −1.43 and 53.71%, respectively. QMEAN is a type of Z-score: values around zero indicate good agreement between model and experimental structures of similar size, and scores of −4.0 or less indicate models of low quality (27). A sequence identity of greater than 40% is preferable when building an appropriate model. The X-ray crystallography structure of bovine HSPA8 was used as the a template for rat HSPA8 (28). The QMEAN score and sequence identity were −0.70 and 99.64%, respectively. Human HSP90 was modeled based on data from cryo-EM (29). The QMEAN score and sequence identity of the model were −1.74 and 86.58%, respectively. Protein–protein docking between each subunit of the homodimeric CLCN2 (green and cyan) and its interaction proteins (wheat and olive) were built in 1:1 stoichiometry using ClusPro 2.0. The weighted energy of the top-ranked cluster was −1690.2 C for the CLCN2–HSP90 interaction, and −1497.8 C for the CLCN2–HSPA8 interaction, indicating enough energies to form protein–protein interactions. The highest priority models for CLCN2–HSPA8 and CLCN2–HSP90 are represented in Figs. 9 and 10, respectively. The anion selectivity filter is indicated in *red* in Figs. 9*A* and 10*A*; the estimated molecular surfaces of both models are overviewed in Figs. 9*B* and 10*B*, and the electrostatically tight interaction between CLCN2 and HSP90 or HSPA8 is shown in a *blue–red* color gradient in Figs. 9*C* and 10*C*. According to the simulation model, HSP90 (Fig. 9, *A–C*) and HSPA8 (Fig. 10, *A–C*) bind to CLCN2 in different ways. HSP90 surrounds CLCN2 and binds to the lateral side of each CLCN2 subunit in 1:1 stoichiometry. The dimer interface remains unaffected (Fig. 9*C*). In contrast, HSPA8 protrudes straight from the boundary part between the two CLCN2 subunits and tightly binds to the interface of the homodimer, *i.e.* one HSPA8 binds to both CLCN2 subunits (Fig. 10*C*).

Discussion

Major findings

This study demonstrates that CLCN2 is functionally expressed in cardiomyocytes and interacts with HSPA8 at the cell membrane. Because other possible proteins that contribute to the hyperpolarization-activated Cl^- current are undetectable, the CLCN2–HSPA8 complex is a leading candidate for the molecular architecture of the previously reported $I_{Cl,h}$. The ClC-2 current induced by the co-transfection of *Clcn2* and *Hspa8* into HEK293 and PC12 cells showed unique $[Cl^-]_i$-dependent properties. Voltage-dependent activation revealed two components with Boltzmann fitting, *i.e.* low- and high-voltage–activated components. Statistical analyses revealed that essential impact of *Hspa8* appears to be the low-voltage–activated component, which shifts to hyperpolarized potentials by increasing $[Cl^-]_i$. $V_{1/2}$ of the high-voltage–activated component and other physiological parameters in the presence of *Hspa8* are hardly different from those in the absence of it.

It is known that as $[Cl^-]_i$ increases, the steady-state activation curve of CLCN2 shifts toward positive potential (Fig. 1, *C–E*) (20), and such $[Cl^-]_i$ dependence is caused by the association of HSP90 with CLCN2. Hinzpeter *et al.* (24) reported that human HSP90 binds to rat CLCN2 in HEK293 cells and that pharmacological inhibition of HSP90 reduced ClC-2 currents and impaired the $[Cl^-]_i$-dependent rightward shift of the fractional conductance. Previously, we recorded a ClC-2–like current, $I_{Cl,h}$, and in this study, we confirmed the expression of CLCN2 in the cells (Figs. 1–5). Interestingly, the activation curve of $I_{Cl,h}$ shifted toward negative potential with increasing $[Cl^-]_i$ values in PV cardiomyocytes. Here, another CLCN2-interacting partner, HSPA8, was identified (Fig. 4). Homology modeling of the protein structure and protein–protein docking simulations demonstrated that both heat-shock proteins,

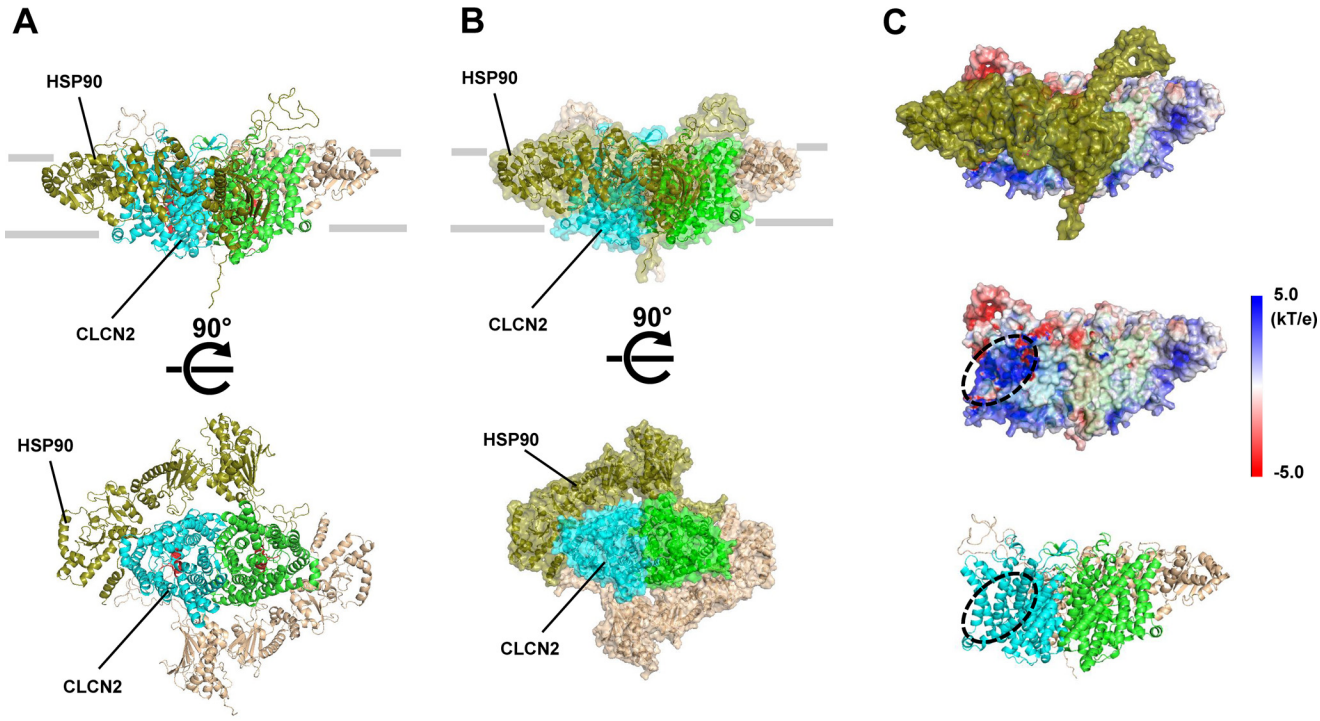

Figure 9. High-throughput simulation of protein–protein docking between rat CLCN2 and human HSP90. Protein structures of CLCN2 (*cyan* and *green*) and HSP90 (*olive* and *wheat*) were homologically modeled by SWISS-MODEL. Docking states were calculated using ClusPro 2.0. The highest priority model is visualized as a cartoon ribbon structure (*A*) and with protein surface (*B*). The *upper panels* in *A* and *B* are side views of the model with a tentative plasma membrane (*gray lines*). The corresponding *lower panels* are bottom views, which illustrate the intracellular side of the subunit assembly. Anion-selective protopore gates are indicated in *red*. *C,* surface electrostatic potential is color-coded by the *kT/e* unit. One of the HSP90 proteins (*olive color* in the *top panel*) is subtracted in the *middle,* displaying an electrostatically strong docking site (*dotted line*). The cartoon structure (*bottom*) indicates that the docking site does not affect the homodimeric interface.

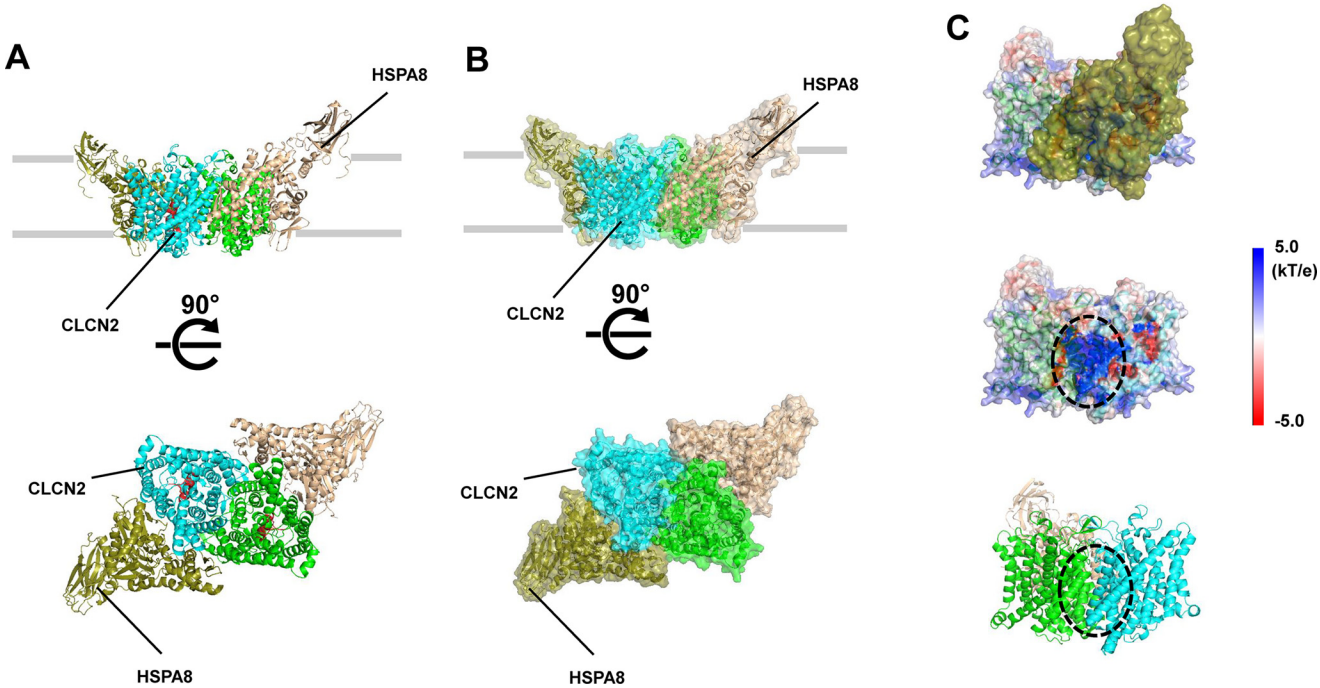

Figure 10. Protein–protein docking between rat CLCN2 and HSPA8. Protein structures of CLCN2 (*cyan* and *green*) and HSPA8 (*olive* and *wheat*) were homologically modeled, and docking states were calculated using ClusPro 2.0. The highest priority model is visualized with a tentative plasma membrane (*gray lines*). The *upper* and *lower panels* in *A* and *B* display side and bottom views, respectively. The anion-selective protopore gates are colored *red*. *C,* surface electrostatic potential is color-coded by the *kT/e* unit. One of the HSPA8 proteins (*olive color* in the *top panel*) is subtracted in the *middle*, displaying an electrostatically strong docking site (*dotted line*). The cartoon structure (*bottom*) indicates that the docking site interacts with the homodimeric interface.

human HSP90 and rat HSPA8, interact with the same channel-pore subunit, CLCN2, but in different ways (Figs. 9 and 10). Each HSP90 binds to one of the dimeric subunits of CLCN2, without affecting the interface of the homodimer (Fig. 9), while HSPA8 binds to both CLCN2s at the boundary between the homodimer subunits. These structural differences may under-

lie the different $[Cl^-]_i$ dependences, *i.e.* the ClC-2 current produced by CLCN2–HSP8 shows a $[Cl^-]_i$-dependent leftward shift in the activation curve, as was observed for $I_{Cl,\,h}$ in LV and PV cardiomyocytes (Fig. 3) (15). However, in this study, we could not perfectly reproduce the $[Cl^-]_i$-dependent leftward shift of the activation curve when *Hspa8* and *Clcn2* were co-transfected into HEK293 or PC12 cells (Figs. 6 and 7). This may indicate that HSPA8 and endogenous CLCN2-interacting proteins, such as HSP90, hinder each other when associating with CLCN2, thereby counteracting the $[Cl^-]_i$-dependent shift of the activation curve. Theoretically, two Boltzmann components suggest that HSPA8 and the other CLCN2-interacting molecules produce two ClC-2 currents with different kinetic properties, one of which is activated at a negative potential, and the other is activated at a more positive potential under high $[Cl^-]_i$ conditions (Fig. 7, *D–G*). In this respect, this study suggests that HEK293 cells use HSP90 as a CLCN2-binding partner, whereas PC12 cells also contain a subunit that is functionally distinct from HSPA8.

CLCN2 belongs to the CLC Cl^- channel/transporter family, which includes homodimeric channels with two independent Cl^- permeation pathways. The negatively-charged carboxyl side chain of a glutamate residue located within the permeation pathway forms a protopore (30). The CLC family possesses two different ionic gates: a fast-acting protopore gate and a slow-acting common gate. The fast gate controls each protopore, and a common gate simultaneously controls both protopores. Detailed mechanisms of these gates are still being debated. It was recently suggested that the voltage-dependent activation of the protopore gates is not governed by the movement of voltage-sensitive domains (31); instead, the hyperpolarization pushes the intracellular Cl^- ions into binding sites within the pore, resulting in the opening of the protopore gate. This hypothesis favors the $[Cl^-]_i$-dependent rightward shift of the activation curve of the ClC-2 current observed in HEK293 cells. Indeed, the CLCN2–HSP90 association (observed in Fig. 9) hardly obstructs the nature of the protopores. At the same time, it has been reported that neutralization of Glu-217, the gating glutamate of guinea pig CLCN2, results in ClC-2 channels without a protopore gate and that the activation curve of these channels shows a rightward shift with decreasing $[Cl^-]_i$ (32). These findings indicate that $[Cl^-]_i$ affects the protopore gate and the common gate in opposite ways and that the overall $[Cl^-]_i$ dependence usually masks the effect on the protopore gate in the case of ClC-2 current. Accordingly, we speculate that HSPA8 affects the $[Cl^-]_i$ dependence by enhancing the $[Cl^-]_i$-dependent property of the common gate. Structural analysis (Fig. 10) indicates that the CLCN2–HSPA8 complex interacts with the dimeric interface across both individual subunits. It is likely that the common gate is stabilized by the CLCN2–HSPA8 interaction, and its characteristics may be unmasked. This finding is consistent with our speculation, and we may safely conclude that HSPA8 is an auxiliary subunit that modulates the $[Cl^-]_i$ dependence of CLCN2.

To the best of our knowledge, this is the first report to identify HSPA8 as an accessory subunit of an ion channel. HSPA8 is a clathrin-uncoating ATPase (33) and is classified as a member the HSP70 family (34). Most HSPs are stress-inducible, whereas HSAP8 constitutively localizes to the cytoplasm and lysosome. As a chaperone protein, HSPA8 is substantially recruited in the cell-cycle G_1/S transition (35, 36), and it positively regulates chaperone-mediated autophagy (37–39). With these cellular functions, HSPA8 is thought to play a crucial role in cell differentiation and embryonic development (40–42). Additionally, the ability of HSPA8 to interact with ion channels on the cell membrane has been reported in the process of ubiquitin-mediated proteasomal degradation. For example, HSPA8 cooperates with co-chaperones, such as the C-terminal heat-shock cognate 70-interacting protein and Bag1, in the ubiquitination of CFTR (43), Kv1.5 (44), and the human ether-a-go-go–related gene K^+ channel (44). In this study, expression of HSPA8 was nearly restricted to the cell surface, and a corresponding co-chaperone was not observed in the Coomassie-stained SDS-polyacrylamide gels (Fig. 4*A*). Thus, HSPA8 is supposed to bind directly to CLCN2 on the membrane and to regulate channel properties rather than engage the maturation of the channel. Hinzpeter *et al.* (24) reported that the association of HSP90 with ClC-2 results in higher channel activity as a result of increased cell-surface channel expression, facilitation of channel opening, and enhanced channel sensitivity to intracellular $[Cl^-]_i$. In this study, *Clcn2* was transiently transfected with or without co-transfection of *Hspa8*, and the level of gene expression was not stably controlled. The density of ClC-2 current in HEK293 and PC12 cells varied from cell to cell (Fig. 8); thus, we could not determine whether HSPA8 aids in the expression of CLCN2 channels. It should be noted that HEK293 and PC12 cells possess CLCN2-interacting proteins, and therefore, the positive effect of HSPA8 on channel expression may have been masked by these endogenous molecules.

Accessory proteins for CLCN2 appear to differ by cell type. In glial cells, CLCN2 interacts with GlialCAM (45), which was originally identified as a major partner of MLC1, the protein responsible for autosomal-recessive inheritance disease megalencephalic leukoencephalopathy with subcortical cysts (46). GlialCAM directs the CLCN2 channel to the cell–cell junctions, enhances the current amplitude (47), and changes the activation properties by affecting the common gate (48). We propose that CLCN2 requires accessory proteins for proper expression and function at cell membranes and that HSPA8 fills this role in the heart.

Limitations

It was considerably challenging to reproduce the same time-dependent kinetics in ClC-2 current in different biological materials, such as *Xenopus* oocytes, cultured cells, and isolated cardiomyocytes. Reportedly, the time constant in activation currents of ClC-2 is $<$200 ms for HEK293 (49), $\sim$2000 ms for cardiomyocytes (18, 19), and $\gg$5000 ms for *Xenopus* oocytes (23). In other words, the activation kinetics are prolonged as the cell size increased. One of the reasons is considered to be the amount of cytoskeleton inside cells. Ahmed *et al.* (23) have reported that disruptions of the cytoskeletons dramatically enhanced the activation process of the current. Further efforts will be required to determine the molecular reasons for cell type–dependent differences in the time dependence of the current.

Conclusions

This study identified an accessory protein of the ClC-2 channel in rat cardiomyocytes. This regulatory protein is likely to be responsible for the molecular characteristics of $I_{Cl,\,h}$ in voltage-dependent gating. The results may contribute to the development of drugs that pharmacologically suppress the hyperpolarization-activated current that precedes diastolic depolarization in arrhythmia.

Materials and methods

Ethical approval

The protocols used in this study were approved by the Animal Ethics Committees of the Yamagata University Faculty of Medicine, Japan, and the Akita University School of Medicine, Japan. All experiments were performed at Yamagata University or Akita University under personal and project licenses following appropriate institutional reviewing.

Preparation of rat hearts

Male Wistar rats (8–14 weeks) were purchased from Charles River Laboratories or CLEA Japan, Inc. To isolate cardiomyocytes from PV and LV, rats were anesthetized by intraperitoneal injection of mixed anesthesia (0.15 mg/kg medetomidine, 2.0 mg/kg midazolam, and 2.5 mg/kg butorphanol). After checking suppression of the nociceptive reflex, the chest cavity was opened under artificial respiration, and the aorta was cannulated *in situ* to perfuse the coronary arteries. The heart and lung were excised in block, mounted on a Langendorff apparatus, and then perfused sequentially with the following buffers: 1) normal Tyrode's solution for ~3 min, to wash blood out from heart and lung; 2) nominally Ca^{2+}-free Tyrode's solution for 5 min; and 3) Ca^{2+}-free Tyrode's solution containing 0.05% (w/v) collagenase and 0.005% (w/v) elastase (Wako Pure Chemicals, Osaka, Japan) for 30 min. The composition of the normal Tyrode's solution was as follows (in mM): NaCl, 136.9; KCl, 5.4; $CaCl_2$, 1.8; $MgCl_2$, 0.5; NaH_2PO_4, 0.33; HEPES, 5.0; and glucose, 5.5 (pH 7.4 adjusted with NaOH). After digestion, the heart was perfused with 50 ml of a high-K^+, low-Cl^- solution composed of the following (in mM): L-glutamic acid, 70; KOH, 70; KCl, 30; KH_2PO_4 10; $MgCl_2$, 1; taurine, 20; glucose, 10; EGTA, 0.3; and HEPES, 10 (pH 7.4 adjusted with KOH). We then trimmed off the soft tissue containing the vagus nerves, adipose tissue, and the pulmonary artery under a stereomicroscope. The LV was dissected, and the left PV was excised from the digested block. The LV and left PV were then minced gently in the high-K^+, low-Cl^- solution before being gently agitated to dissociate the cells. The two cell suspensions were stored at 4 °C for later use.

PV preparation for molecular cloning of *Clcn2* was obtained by a similar procedure to that described above, except that the enzymatic digestion was not performed. In this study, samples of PV were collected from regions, including PV ostia and the left PV trunk.

Molecular cloning of Clcn2 and Hspa8 from rat PV cardiomyocytes

Total RNA was extracted from rat PV using a RNeasy mini kit (Qiagen, Hilden, Germany). cDNA was transcribed using a PrimeScript II 1st Strand cDNA synthesis kit (Takara Bio Inc., Kusatsu, Japan). The *Clcn2* and *Hspa8* complete coding sequences were then amplified from the extracted cDNA using specific primers (see Table 1) containing HindIII and EcoRI and EcoRI and XbaI restriction sites, respectively. The following thermal cycler protocol was used to amplify the cDNA regions: 35 cycles of 98 °C for 10 s, 55 °C for 5 s, and 72 °C for 3 min, followed by a final extension at 72 °C for 7 min. All reactions were performed in a Dice thermal cycler (Takara). Amplicons were gel-purified and subcloned into the pcDNA3.1 vector (Thermo Fisher Scientific, Waltham, MA) using the appropriate restriction enzymes and a DNA ligation kit, Long (Takara). Recombinant plasmids were purified, and their DNA sequences were confirmed by Sanger sequencing (model 310; Applied Biosystems, Foster City, CA).

Table 2
Composition of internal solutions used in Cl^- current recording
Solution 1 is $[Cl^-]_i$ = 40 mM; solution 2 is $[Cl^-]_i$ = 100 mM; and solution 3 is $[Cl^-]_i$ = 150 mM. The pH value of all internal solutions was adjusted with CsOH.

	Internal solutions		
	1	2	3
CsCl	30.0	90.0	140.0
CsOH	110.0	50.0	
Aspartic acid	110.0	50.0	
Na_2-ATP	5.0	5.0	5.0
$MgCl_2$	5.0	5.0	5.0
EGTA	5.0	5.0	5.0
HEPES	5.0	5.0	5.0
GTP-Na_2	0.1	0.1	0.1

Transfection of Clcn2 and Hspa8 into HEK293 and PC12 cells

For functional analysis, cloned *Clcn2* was transiently transfected with or without subcloned *Hspa8* into HEK293 and PC12 cells using Lipofectamine 2000 transfection reagent (Thermo Fisher Scientific) according to the manufacturer's instructions. Enhanced green fluorescence protein was co-transfected to label transfected cells. The transfection efficiency was 40–50%. Cells were settled on poly-D-lysine–coated coverslips and subcultured for 48 h prior to electrophysiological recording.

Electrophysiological analysis by patch-clamping

The whole-cell patch-clamp method was used to record membrane currents (patch-clamp amplifier Axopatch 200B; Molecular Devices, Chicago). Borosilicate glass electrodes had tip resistances between 2.0 and 5.0 megohms when filled with internal solution. For Cl^- current recording, KCl of Tyrode's solution was substituted by equimolar CsCl. Membrane currents were recorded under voltage-clamp conditions at 37 ± 1 °C. Pulse protocols and data acquisition and storage were managed using CLAMPEX (Molecular Devices). The sampling frequency was 1 kHz and low-pass filtering was performed at 500 Hz. The cell membrane capacitance was determined by applying a 30-ms hyperpolarizing voltage-clamp step from a holding potential of 0 to −5 mV and integrating the area under the capacitive transient. All patch-clamp data were analyzed using IGOR software (Wavemetrics, Portland, OR). The junction potential between Cs-Tyrode's solution and the intracellular solution were corrected numerically using previously measured values (15), because solutions used in this study were identical. The compositions of internal solutions for recording Cl^- currents are presented in Table 2. To evaluate

the voltage-dependent current availability, the current was activated by applying 2-s hyperpolarizing pulses to various test potentials from the holding potential of 0 mV, followed by depolarization to 40 mV. The relationship between the test potentials and the relative amplitude of the tail current was fitted using Boltzmann Equation 1,

$$I/I_{Max} = \frac{1}{1 + \exp\left\{-\left(\frac{V_m - V_{1/2}}{S}\right)\right\}} \quad \text{(Eq. 1)}$$

where I_{Max} is the predicted maximum current amplitude; V_m is the membrane voltage; S is the scaling factor; and $V_{1/2}$ is the V_m needed to reach half the I/I_{Max}. Summations of two Boltzmann functions were applied to analyze the activation curves of two-component currents in HSPA8-expressing cells. Time-dependent kinetics of the $I_{Cl,\,h}$ of LV cardiomyocytes was analyzed by fitting the current with a first-order biexponential function as shown in Equation 2,

$$I(t) = y_1\left\{1 - \exp\left(-\frac{t}{\tau_{fast}}\right)\right\} + y_2\left\{1 - \exp\left(-\frac{t}{\tau_{slow}}\right)\right\} + y_0 \quad \text{(Eq. 2)}$$

where τ_{fast} and τ_{slow} are fast and slow time constants, respectively.

Immunocytochemistry and confocal imaging

Isolated PV and LV cardiomyocytes settled on poly-D-lysine–coated coverslips were incubated for 30 min at room temperature and subsequently fixed with 4% paraformaldehyde for 30 min at room temperature. The cells were then permeabilized using PBS containing 0.2% (w/v) Triton X-100 for 15 min and subsequently incubated with blocking buffer (PBS containing 5% BSA). Cells were then stained with antibodies against ryanodine receptor (RyR; Abcam, Cambridge, UK; catalog no. ab2827), Na/K pump (Abcam, catalog no. ab76020), CLCN2 (Santa Cruz Biotechnology, Dallas, TX, catalog no. sc-377284; Alomone Labs, Jerusalem, Israel, catalog no. ACL-002), and HSPA8 (Abcam; catalog no. ab2788). All primary antibodies were diluted 1:500 in antibody buffer/PBS containing 1% (w/v) BSA. Appropriate secondary antibodies were then used (either anti-mouse or anti-rabbit, conjugated with either Alexa Fluor 488 or Alexa Fluor 594) at a 1:1000 dilution. Cells were mounted on glass slides using Permount (Thermo Fisher Scientific, Hampton, NH). Single-slice and/or image stacks were obtained using a Zeiss 700 confocal microscope (×63, pinhole size of an arbitrary unit). Captured images were processed using ZEN Image software (Zeiss).

Co-immunoprecipitation and MS

To prepare crude membrane protein fractions from rat hearts, the LV and PV were dissected from rats as described above in Ca^{2+}-free Tyrode's solution at 4 °C and then flash-frozen in liquid nitrogen before being stored at −80 °C for later use. To extract membrane proteins, the heart samples were resuspended in a solution containing 50 mM Tris-HCl (pH 7.5), 250 mM sucrose, and proteinase inhibitor mixture (cOmplete Mini, Thermo Fisher Scientific) and then homogenized. The homogenates were centrifuged at 800 × *g* for 10 min to remove the nuclear proteins and then recentrifuged at 15,000 × *g* for 15 min to remove lysosomes and mitochondria. Supernatants were pelleted at 100,000 × *g* for 1 h at 4 °C. The resultant pellets were used as the plasma membrane–enriched fraction. For solubilization, the pellets were incubated for 1 h at 4 °C in cell lysis buffer composed of 10 mM Tris (pH 7.5), 1% (w/v) Triton X-100, 150 mM NaCl, 5 mM EDTA, 10% glycerol, and proteinase inhibitor mixture. Aliquots (0.5 ml) of the solubilized samples containing membrane proteins (500 or 1000 μg quantified by the Bradford assay) were incubated for 1 h with 2 μg of mouse anti-CLCN2 (Santa Cruz Biotechnology, catalog no. sc-377284) or rabbit anti-HSPA8 (Proteintech, Chicago; catalog no. 10654-1-AP) coupled with Dynabeads protein G superparamagnetic beads (Thermo Fisher Scientific). Precipitants with 10 μg of normal mouse or rabbit IgG were used as negative controls. After being washed three times, bound proteins were eluted in Laemmli buffer and run on 10% SDS-polyacrylamide gels. For LC-tandem MS analysis (LC-MS/MS), Coomassie Brilliant Blue-stained gel lanes were excised, and proteins were digested with high-grade trypsin (Promega, Fitchburg, WI). Trypsinized peptides were resolved in 0.5% TFA and then loaded onto a pre-column (C18 PepMap100, 5 μm; Dionex, Idstein, Germany). After demineralization of the loaded sample, LC was performed on an EASY-nLC1000 LC system (Thermo Fisher Scientific) and directly electrosprayed into a Q-Exactive mass spectrometer (Thermo Fisher Scientific). MS/MS spectra were analyzed using Proteome Discoverer 1.3 (Thermo Fisher Scientific).

SDS-PAGE and western blotting

Proteins extracted from PV, LV, and PC12 cells were separated by electrophoresis on 10% SDS-polyacrylamide gels using the Mini-PROTEAN system (Bio-Rad) and then transferred onto polyvinylidene fluoride membranes. The membranes were blotted using mouse anti-CLCN2 (Santa Cruz Biotechnology, catalog no. sc-377284) or rabbit anti-HSPA8 (Proteintech, catalog no. 10654-1-AP) primary antibodies at a 1:1000 dilution. Appropriate secondary antibodies were then used (either anti-mouse or anti-rabbit, conjugated with horseradish peroxidase (HRP), at 1:10,000 dilution)). Housekeeping protein GAPDH was blotted using anti-GAPDH antibody (Cell Signaling, catalog no. 2118), if necessary. The HRP reaction was carried out using ECL Prime Detection Reagent (GE Healthcare). Results were visualized using a ChemiDoc XRS 255 imaging system (Bio-Rad) or ImageStation 2000R (Eastman Kodak Co.).

Homology modeling of protein structure and protein–protein docking simulation

Template-based homology modeling of rat CLCN2 and HSPA8 was performed using the SWISS-MODEL bioinformatic modeling server (https://swissmodel.expasy.org/). Human CLC-1 (26) and HSP90 (29) and bovine HSPA8 (28) were used as templates. Protein models were simulated as both dimers and monomers, downloaded as PDB files, and uploaded to Cluspro

2.0 (https://cluspro.org/).[3] This computer server calculates interaction energies of billions of conformation models and outputs 10 protein–protein docking states. The top-ranked docking state was used as the CLCN2–HSPA8 docking model. The model was visualized using PyMOL software (Schrödinger, LLC).

Statistical analysis

Results are expressed as the mean ± S.E. The number of cells (n) used in each experiment is indicated in the figures and text. Statistical significance was determined using Mann-Whitney's U-tests, one-way ANOVA, Kruskal-Wallis test, or two-way ANOVA appropriately using Prism 8.1.0 (GraphPad Software, San Diego). A p value less than 0.05 was considered statistically significant and indicated with an asterisk in figures.

Author contributions—Y. Okamoto, Y. N., K. I., and K. O. conceptualization; Y. Okamoto resources; Y. Okamoto and Y. N. data curation; Y. Okamoto formal analysis; Y. Okamoto funding acquisition; Y. Okamoto investigation; Y. Okamoto, Y. N., Y. Obara, K. I., and D. T. methodology; Y. Okamoto and K. O. writing original draft; K. O. supervision; K. O. project administration; K. O. writing review and editing.

Acknowledgments—We thank Dr. Yuko Kozasa (Kurume University) for helpful comments and encouragement, and we thank Hayden Peacock (Edanz Group) for editing a draft of this manuscript.

References

1. Haïssaguerre, M., Jaïs, P., Shah, D. C., Takahashi, A., Hocini, M., Quiniou, G., Garrigue, S., Le Mouroux, A., Le Métayer, P., and Clémenty, J. (1998) Spontaneous initiation of atrial fibrillation by ectopic beats originating in the pulmonary veins. *N. Engl. J. Med.* **339,** 659–666 CrossRef Medline
2. Chugh, S. S., Havmoeller, R., Narayanan, K., Singh, D., Rienstra, M., Benjamin, E. J., Gillum, R. F., Kim, Y. H., McAnulty, J. H., Jr., Zheng, Z. J., Forouzanfar, M. H., Naghavi, M., Mensah, G. A., Ezzati, M., and Murray, C. J. (2014) Worldwide epidemiology of atrial fibrillation: a global burden of disease 2010 study. *Circulation* **129,** 837–847 CrossRef Medline
3. Cheung, D. W. (1981) Electrical activity of the pulmonary vein and its interaction with the right atrium in the guinea pig. *J. Physiol.* **314,** 445–456 CrossRef Medline
4. Doisne, N., Maupoil, V., Cosnay, P., and Findlay, I. (2009) Catecholaminergic automatic activity in the rat pulmonary vein: electrophysiological differences between cardiac muscle in the left atrium and pulmonary vein. *Am. J. Physiol. Heart Circ. Physiol.* **297,** H102–H108 CrossRef Medline
5. Okamoto, Y., Takano, M., Ohba, T., and Ono, K. (2012) Arrhythmogenic coupling between the Na^+–Ca^{2+} exchanger and inositol 1,4,5-triphosphate receptor in rat pulmonary vein cardiomyocytes. *J. Mol. Cell. Cardiol.* **52,** 988–997 CrossRef Medline
6. Cheung, D. W. (1981) Pulmonary vein as an ectopic focus in digitalis-induced arrhythmia. *Nature* **294,** 582–584 CrossRef Medline
7. Sood, S., Chelu, M. G., van Oort, R. J., Skapura, D., Santonastasi, M., Dobrev, D., and Wehrens, X. H. (2008) Intracellular calcium leak due to FKBP12.6 deficiency in mice facilitates the inducibility of atrial fibrillation. *Heart Rhythm.* **5,** 1047–1054 CrossRef Medline
8. Goette, A., Staack, T., Röcken, C., Arndt, M., Geller, J. C., Huth, C., Ansorge, S., Klein, H. U., and Lendeckel, U. (2000) Increased expression of extracellular signal-regulated kinase and angiotensin-converting enzyme in human atria during atrial fibrillation. *J. Am. Coll. Cardiol.* **35,** 1669–1677 CrossRef Medline
9. Shiroshita-Takeshita, A., Brundel, B. J., Burstein, B., Leung, T. K., Mitamura, H., Ogawa, S., and Nattel, S. (2007) Effects of simvastatin on the development of the atrial fibrillation substrate in dogs with congestive heart failure. *Cardiovasc. Res.* **74,** 75–84 CrossRef Medline
10. Zhang, D., Chen, X., Wang, Q., Wu, S., Zheng, Y., and Liu, X. (2017) Role of the MAPKs/TGF-β1/TRAF6 signaling pathway in postoperative atrial fibrillation. *PLoS ONE* **12,** 1–12 CrossRef
11. Lian, H., Wang, X., Wang, J., Liu, N., Zhang, L., Lu, Y., Yang, Y., and Zhang, L. (2015) Heart-specific overexpression of (pro)renin receptor induces atrial fibrillation in mice. *Int. J. Cardiol.* **184,** 28–35 CrossRef Medline
12. Li, M., Yi, X., Ma, L., and Zhou, Y. (2013) Hepatocyte growth factor and basic fibroblast growth factor regulate atrial fibrosis in patients with atrial fibrillation and rheumatic heart disease via the mitogen-activated protein kinase signaling pathway. *Exp. Ther. Med.* **6,** 1121–1126 CrossRef Medline
13. Ellinor, P. T., Lunetta, K. L., Albert, C. M., Glazer, N. L., Ritchie, M. D., Smith, A. V., Arking, D. E., Müller-Nurasyid, M., Krijthe, B. P., Lubitz, S. A., Bis, J. C., Chung, M. K., Dörr, M., Ozaki, K., Roberts, J. D. *et al.* (2012) Meta-analysis identifies six new susceptibility loci for atrial fibrillation. *Nat. Genet.* **44,** 670–675 CrossRef Medline
14. Harada, M., Luo, X., Qi, X. Y., Tadevosyan, A., Maguy, A., Ordog, B., Ledoux, J., Kato, T., Naud, P., Voigt, N., Shi, Y., Kamiya, K., Murohara, T., Kodama, I., Tardif, J. C., *et al.* (2012) Transient receptor potential canonical-3 channel-dependent fibroblast regulation in atrial fibrillation. *Circulation* **126,** 2051–2064 CrossRef Medline
15. Okamoto, Y., Kawamura, K., Nakamura, Y., and Ono, K. (2014) Pathological impact of hyperpolarization-activated chloride current peculiar to rat pulmonary vein cardiomyocytes. *J. Mol. Cell. Cardiol.* **66,** 53–62 CrossRef Medline
16. Levesque, P. C., Hart, P. J., Hume, J. R., Kenyon, J. L., and Horowitz, B. (1992) Expression of cystic fibrosis transmembrane regulator Cl^- channels in heart. *Circ. Res.* **71,** 1002–1007 CrossRef Medline
17. Verkerk, A. O., Veldkamp, M. W., Bouman, L. N., and van Ginneken, A. C. (2000) Calcium-activated Cl^- current contributes to delayed after depolarizations in single Purkinje and ventricular myocytes. *Circulation* **101,** 2639–2644 CrossRef Medline
18. Duan, D., Ye, L., Britton, F., Horowitz, B., and Hume, J. R. (2000) A novel anionic inward rectifier in native cardiac myocytes. *Circ. Res.* **86,** E63–E71 Medline
19. Britton, F. C., Wang, G.-L., Huang, Z. M., Ye, L., Horowitz, B., Hume, J. R., and Duan, D. (2005) Functional characterization of novel alternatively spliced ClC-2 chloride channel variants in the heart. *J. Biol. Chem.* **280,** 25871–25880 CrossRef Medline
20. Sánchez-Rodríguez, J. E., De Santiago-Castillo, J. A., and Arreola, J. (2010) Permeant anions contribute to voltage dependence of ClC-2 chloride channel by interacting with the protopore gate. *J. Physiol.* **588,** 2545–2556 CrossRef Medline
21. Britton, F. C., Hatton, W. J., Rossow, C. F., Duan, D., Hume, J. R., and Horowitz, B. (2000) Molecular distribution of volume-regulated chloride channels (ClC-2 and ClC-3) in cardiac tissues. *Am. J. Physiol. Heart Circ. Physiol.* **279,** H2225–H2233 CrossRef Medline
22. Clark, S., Jordt, S. E., Jentsch, T. J., and Mathie, A. (1998) Characterization of the hyperpolarization-activated chloride current in dissociated rat sympathetic neurons. *J. Physiol.* **506,** 665–678 CrossRef Medline
23. Ahmed, N., Ramjeesingh, M., Wong, S., Varga, A., Garami, E., and Bear, C. E. (2000) Chloride channel activity of ClC-2 is modified by the actin cytoskeleton. *Biochem. J.* **352,** 789–794 Medline
24. Hinzpeter, A., Lipecka, J., Brouillard, F., Baudoin-Legros, M., Dadlez, M., Edelman, A., and Fritsch, J. (2006) Association between Hsp90 and the ClC-2 chloride channel upregulates channel function. *Am. J. Physiol. Cell Physiol.* **290,** C45–C56 CrossRef Medline
25. Kashino, Y., Obara, Y., Okamoto, Y., Saneyoshi, T., Hayashi, Y., and Ishii, K. (2018) ERK5 phosphorylates Kv4.2 and inhibits inactivation of the A-type current in PC12 cells. *Int. J. Mol. Sci.* **19,** 2008 CrossRef Medline
26. Park, E., and MacKinnon, R. (2018) Structure of the CLC-1 chloride channel from *Homo sapiens*. *Elife* **7,** 1–24 CrossRef
27. Benkert, P., Biasini, M., and Schwede, T. (2011) Toward the estimation of the absolute quality of individual protein structure models. *Bioinformatics* **27,** 343–350 CrossRef Medline

[3] Please note that the JBC is not responsible for the long-term archiving and maintenance of this site or any other third party hosted site.

28. Jiang, J., Prasad, K., Lafer, E. M., and Sousa, R. (2005) Structural basis of interdomain communication in the Hsc70 chaperone. *Mol. Cell.* **20,** 513–524 CrossRef Medline
29. Verba, K. A., Wang, R. Y., Arakawa, A., Liu, Y., Shirouzu, M., Yokoyama, S., and Agard, D. A. (2016) Atomic structure of Hsp90–Cdc37–Cdk4 reveals that Hsp90 traps and stabilizes an unfolded kinase. *Science* **352,** 1542–1547 CrossRef Medline
30. Dutzler, R., Campbell, E. B., Cadene, M., Chait, B. T., and MacKinnon, R. (2002) X-ray structure of a ClC chloride channel at 3.0 A reveals the molecular basis of anion selectivity. *Nature* **415,** 287–294 CrossRef Medline
31. De Jesús Pérez, J. J., Castro-Chong, A., Shieh, R., Hernández Carballo, C. Y., de Santiago Castillos, J. A., and Arreola, J. (2016) Gating the glutamate gate of CLC-2 chloride channel by pore occupancy. *J. Gen. Physiol.* **1,** 25–37 CrossRef Medline
32. Niemeyer, M. I., Cid, L. P., Zúñiga, L., Catalán, M., and Sepúlveda, F. V. (2003) A conserved pore-lining glutamate as a voltage- and chloride-dependent gate in the ClC-2 chloride channel. *J. Physiol.* **553,** 873–879 CrossRef Medline
33. Davis, J. Q., and Bennett, V. (1985) Human erythrocyte clathrin and clatrin-uncoating protein. *J. Biol. Chem.* **260,** 14850–14856 Medline
34. Chappell, T. G., Welch, W. J., Schlossman, D. M., Palter, K. B., Schlesinger, M. J., and Rothman, J. E. (1986) Uncoating ATPase is a member of the 70 kilodalton family of stress proteins. *Cell* **45,** 3–13 CrossRef Medline
35. Gevers, M., Fracella, F., and Rensing, L. (1997) Nuclear translocation of constitutive heat-shock protein 70 during S phase in synchronous macroplasmodia of *Physarum polycephalum*. *FEMS Microbiol. Lett.* **152,** 89–94 CrossRef Medline
36. Diehl, J. A., Yang, W., Rimerman, R. A., Xiao, H., and Emili, A. (2003) Hsc70 regulates accumulation of cyclin D1 and cyclin D1-dependent protein kinase. *Mol. Cell. Biol.* **23,** 1764–1774 CrossRef Medline
37. Yang, Q., She, H., Gearing, M., Colla, E., Lee, M., Shacka, J. J., and Mao, Z. (2009) Regulation of neuronal survival factor MEF2D by chaperone-mediated autophagy. *Science* **323,** 124–127 CrossRef Medline
38. Mak, S. K., McCormack, A. L., Manning-Bog, A. B., Cuervo, A. M., and Di Monte, D. A. (2010) Lysosomal degradation of α-synuclein *in vivo*. *J. Biol. Chem.* **285,** 13621–13629 CrossRef Medline
39. Hubbi, M. E., Hu H., Kshitiz Ahmed, I., Levchenko, A., and Semenza, G. L. (2013) Chaperone-mediated autophagy targets hypoxia-inducible factor-1α (HIF-1α) for lysosomal degradation. *J. Biol. Chem.* **288,** 10703–10714 CrossRef Medline
40. Patterson, S. T., Li, J., Kang, J. A., Wickrema, A., Williams, D. B., and Reithmeier, R. A. (2009) Loss of specific chaperones involved in membrane glycoprotein biosynthesis during the maturation of human erythroid progenitor cells. *J. Biol. Chem.* **284,** 14547–14557 CrossRef Medline
41. Faucette, A. N., Maher, V. A., Gutierrez, M. A., Jucker, J. M., Yates, D. C., Welsh, T. H., Jr., Amstalden, M., Newton, G. R., Nuti, L. C., Forrest, D. W., and Ing, N. H. (2014) Temporal changes in histomorphology and gene expression in goat testes during postnatal development. *J. Anim. Sci.* **92,** 4440–4448 CrossRef Medline
42. DeGeer, J., Kaplan, A., Mattar, P., Morabito, M., Stochaj, U., Kennedy, T. E., Debant, A., Cayouette, M., Fournier, A. E., and Lamarche-Vane, N. (2015) Hsc70 chaperone activity underlies Trio GEF function in axon growth and guidance induced by netrin-1. *J. Cell Biol.* **210,** 817–832 CrossRef Medline
43. Meacham, G. C., Patterson, C., Zhang, W., Younger, J. M., and Cyr, D. M. (2001) The Hsc70 co-chaperone CHIP targets immature CFTR for proteasomal degradation. *Nat. Cell Biol.* **3,** 100–105 CrossRef Medline
44. Li, P., Kurata, Y., Maharani, N., Mahati, E., Higaki, K., Hasegawa, A., Shirayoshi, Y., Yoshida, A., Kondo, T., Kurozawa, Y., Yamamoto, K., Ninomiya, H., and Hisatome, I. (2015) E3 ligase CHIP and Hsc70 regulate Kv1.5 protein expression and function in mammalian cells. *J. Mol. Cell. Cardiol.* **86,** 138–146 CrossRef Medline
45. Jeworutzki, E., López-Hernández, T., Capdevila-Nortes, X., Sirisi, S., Bengtsson, L., Montolio, M., Zifarelli, G., Arnedo, T., Müller, C. S., Schulte, U., Nunes, V., Martínez, A., Jentsch, T. J., Gasull, X., Pusch, M., and Estévez, R. (2012) GlialCAM, a protein defective in a leukodystrophy, serves as a ClC-2 Cl^- channel auxiliary subunit. *Neuron* **73,** 951–961 CrossRef Medline
46. Leegwater, P. A., Yuan, B. Q., van der Steen, J., Mulders, J., Könst, A. A., Boor, P. K., Mejaski-Bosnjak, V., van der Maarel, S. M., Frants, R. R., Oudejans, C. B., Schutgens, R. B., Pronk, J. C., and van der Knaap, M. S. (2001) Mutations of MLC1 (KIAA0027), encoding a putative membrane protein, cause megalencephalic leukoencephalopathy with subcortical cysts. *Am. J. Hum. Genet.* **68,** 831–838 CrossRef Medline
47. Capdevila-Nortes, X., Jeworutzki, E., Elorza-Vidal, X., Barrallo-Gimeno, A., Pusch, M., and Estévez, R. (2015) Structural determinants of interaction, trafficking and function in the ClC-2/MLC1 subunit GlialCAM involved in leukodystrophy. *J. Physiol.* **593,** 4165–4180 CrossRef Medline
48. Jeworutzki, E., Lagostena, L., Elorza-Vidal, X., López-Hernández Estévez, R., and Pusch, M. (2014) GlialCAM, a CLC-2 Cl^- channel subunit, activates the slow gate of CLC chloride channels. *Biophys. J.* **107,** 1105–1116 CrossRef Medline
49. Yamada, T., Krzeminski, M., Bozoky, Z., Forman-Kay, J. D., and Strange, K. (2016) Role of CBS and Bateman domains in phosphorylation-dependent regulation of a CLC anion channel. *Biophys. J.* **111,** 1876–1886 CrossRef Medline